Accepted Manuscript

Pressure-impulse diagrams for elastoplastic beams subjected to pulse-pressure loading

Ye Yuan, Ling Zhu, Xueyu Bai, T.X. Yu, Yibing Li, P.J. Tan

PII: S0020-7683(18)30423-2
DOI: https://doi.org/10.1016/j.ijsolstr.2018.10.021
Reference: SAS 10155

To appear in: *International Journal of Solids and Structures*

Received date: 23 March 2018
Revised date: 4 October 2018
Accepted date: 23 October 2018

Please cite this article as: Ye Yuan, Ling Zhu, Xueyu Bai, T.X. Yu, Yibing Li, P.J. Tan, Pressure-impulse diagrams for elastoplastic beams subjected to pulse-pressure loading, *International Journal of Solids and Structures* (2018), doi: https://doi.org/10.1016/j.ijsolstr.2018.10.021

Pressure-impulse diagrams for elastoplastic beams subjected to pulse-pressure loading

Ye Yuan[a,b], Ling Zhu[c], Xueyu Bai[c], T.X. Yu[c,d], Yibing Li[a], P.J. Tan[b*]

[a] *State Key Laboratory of Automotive Safety & Energy, Department of Automotive Engineering, Tsinghua University, Beijing, PR China*

[b] *Department of Mechanical Engineering, University College London, Torrington Place, London, UK*

[c] *Key Laboratory of High Performance Ship Technology of Ministry of Education, School of Transportation, Wuhan University of Technology, Wuhan, PR China*

[d] *Department of Mechanical and Aerospace Engineering, The Hong Kong University of Science and Technology, Clear Water Bay, Kowloon, Hong Kong, PR China*

Abstract

Pressure-impulse (or p-I) diagrams are developed for fully-clamped elastic-plastic beams subjected to pulse-pressure loading with varying degree of negative phase. Unlike traditional p-I diagrams, the loading parameter space are instead divided into régimes, corresponding to the three modes of deformation (I, II and III) observed in blast experiments. The effects of pulse shape, beam aspect ratio and negative phase loading on the isodamage curves that delineate the different régimes are investigated. In addition, it is further demonstrated that contour lines of structural performance (maximum deflection, total work done, partitioned energy and saturated) can also be incorporated into the non-dimensionalised pressure-impulse space to provide further information for the design, and assessment, of elastic-plastic beams to blast loading.

Keywords: Pressure-impulse diagram, deformation régimes, negative phase, saturated impulse

1. Introduction

The pressure-impulse, or p-I for brevity, diagram is a useful design tool that allows quick assessment of the dynamic response of a structural component (typically its final state

*Corresponding author
Email addresses: ye.yuan.10@alumni.ucl.ac.uk (Ye Yuan[a,b]), pj.tan@ucl.ac.uk (P.J. Tan[b])

rather than the response history) to a specified load case. They are typically generated using a simplified single-degree-of-freedom (SDOF) model, whereupon once the maximum displacement (or permissible damage level) has been defined, the p-I space is divided into region(s), corresponding to different régimes, which gives the combinations of load and impulse that are safe or, would otherwise, cause failure (or a specific damage level). A large body of literature already exists on various aspects of constructing p-I diagrams and their features, the majority of which is based on a maximum structural deflection criterion, i.e. it assumes that a structure always deforms in mode I (Abrahamson and Lindberg, 1976; Li and Meng, 2002a,b; Dragos and Wu, 2013; Hamra et al., 2015; Ma et al., 2007; Tsai and Krauthammer, 2017). However, experiments by Menkes and Opat (1973) have showed that a fully clamped beam subjected to a blast load can develop three different modes of deformation: mode I - large inelastic deformation; mode II - tensile-tearing at the support; mode III - shear-band localisation. Unlike in mode I, failure (this is accompanied by complete detachment from the supports) occurs in modes II and III. Hitherto, no work has been done to incorporate information relating to modes II and III deformation in existing p-I diagrams.

Nomenclature

B	width of beam
D	damage variable
E	Young's modulus
E_S^b, E_S^m, E_S^s	bending, membrane, shear energy absorbed at the support
E^P	total work done
H	thickness of beam
I^+, I^-	positive and negative impulse
I^*	non-dimensional impulse
I^*_{sat}	non-dimensional saturated impulse
L	half length of beam
M	bending moment
M_0	fully plastic bending moment
N	membrane force
N_0	fully plastic membrane force
$p(t)$	overpressure time-history
p_c	fully plastic collapse force per unit length
p_0	peak overpressure
p^*	p_0/p_c
Q	transverse shear force
N_0	fully plastic transverse shear force
t	time
t_d, t_d^-	positive and negative phase duration
t_1, t_2	time when plastic hinge form at support and mid-span of beam
t_3	time when beam motion ceases or damage occurs

w_i	generalised transverse displacements
W_B	mid-span deflection
W_0	maximum mid-span deflection
W_S	plastic shear sliding distance at support
α	decay coefficient
β	ratio of the plastic work absorbed through shearing deformation to the total plastic work done
β_c	critical value of β to separate mode II and III
ϵ_{eff}	effective strain
ϵ_d	effective strain at the onset of damage
ϵ_{r}	rupture strain
$\phi_i(x)$	admissible mode functions
ω_s	state variable for shear criterion
ρ	density of beam
σ_Y	static yield strength
ξ	position of the travelling plastic hinge

In this paper, we develop *p*-*I* diagrams, using the model of a fully-clamped ductile beam system by Yuan et al. (2016), to account for the three different modes of deformation and negative phase loading. In addition, we will demonstrate how contour lines of structural performance (maximum deflection, total work done, partitioned energy and saturated) can also be incorporated into the loading parameters space to provide further information for the design, and assessment, of elastic-plastic beams to blast loading.

The outline of this paper is as follows: Section 2 summarises key features of the ductile beam model in Yuan et al. (2016) and the generation of pulse-pressures with varying negative phase; *p*-*I* diagrams are generation in Section 3 and effects of negative phase loading on the isodamage curves discussed; and, finally Section 4 shows how contour lines of structural performance can be incorporated into the diagrams.

2. Method

A succinct summary of key features of the ductile beam model by Yuan et al. (2016) is given here. Its predictive capabilities had previously been successfully validated against results from blast experiments and three-dimensional finite element simulations. For completeness, we also review how pulse-pressures with both the positive and negative phases are generated; and, the selection criteria for the loading parameters to be represented in the new *p*-*I* diagrams.

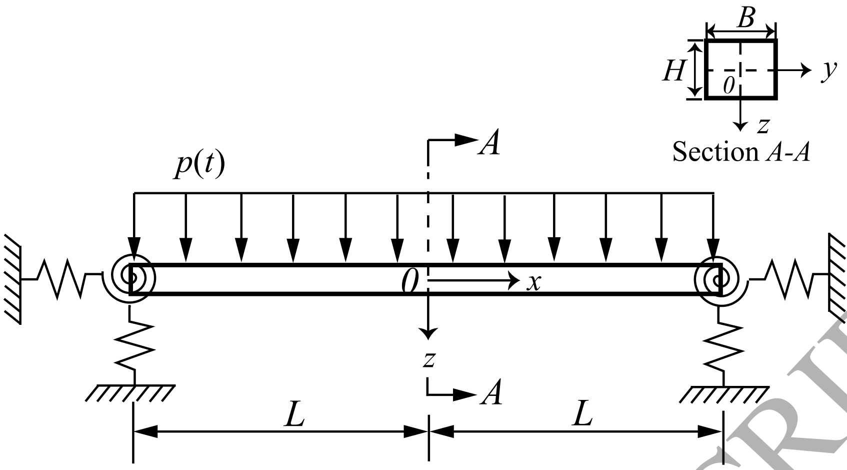

Figure 1: Schematic of the ductile beam system (Yuan et al., 2016).

2.1. Structural model - a summary

Figure 1 shows a schematic of the ductile beam system which comprises a slender beam (made of a rate-independent, elastic perfectly-plastic material) supported at each end by three springs, one rotational and two axials. The two torsional 'elasto-plastic' springs model the end rotation of the beam and the subsequent formation of plastic hinges. Both axial and vertical springs have 'rigid-plastic' characteristics to model plastic stretch and plastic shear sliding at the support, respectively. A pulse-pressure loading $p(t)$, see Section 2.2, impinges normally, and uniformly, over the full span of the beam regardless of its subsequent transverse 'in-plane' motion.

The deformation of the beam is divided into three phases - see Fig. 2 - according to the sequence of hinge formation: (a) Phase 1 ($0 < t \leq t_1$) - no plastic hinge forms anywhere along the beam; (b) Phase 2 ($t_1 < t \leq t_2$) - a stationary plastic hinge forms at the support on each end of the beam; (c) Phase 3 ($t_2 < t \leq t_3$) - plastic hinge A travels towards, and coalesce with, an existing stationary hinge at the mid-span, ending in a final three-hinge collapse configuration. In each phase, the transverse beam deflection is approximated as a sum of n generalised displacements $w_i(t)$ and admissible mode functions $\phi_i(x)$. Once the total strain energy V of each phase is derived, the governing equations of motions for the beam system are obtained by substituting the Lagrangian into the well-known Euler-Lagrange equation – details are given in Yuan et al. (2016). It must be emphasised that the analytical model does not consider the subsequent elastic rebound beyond the maximum mid-span deflection (at $t = t_3$) - the justification for this is provided in Section 2.3.

The structural model implements gradual softening of the non-dimensional bending moment $\bar{M}$, membrane force $\bar{N}$ and transverse shear force $\bar{Q}$ as a function of effective strain ϵ_{eff}.

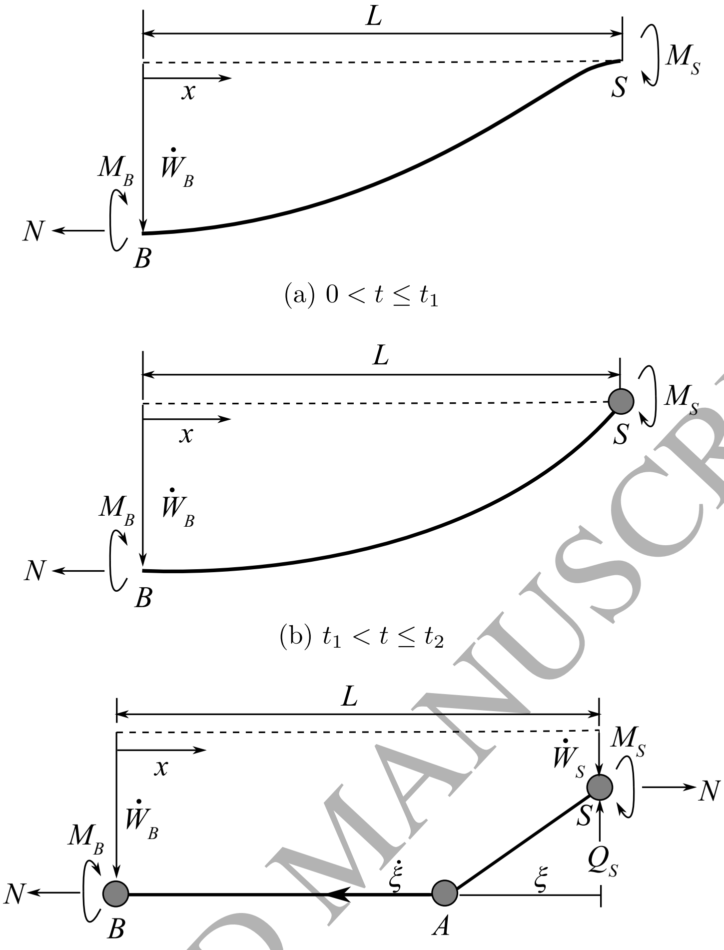

(c) $t_2 < t \leq t_3$

Figure 2: Schematic of the transverse displacement (W_B) profile for the right-half of the ductile beam system in Yuan et al. (2016). (a), (b) and (c) depicts Phases 1, 2 and 3 deformation, respectively. Subscripts S and B denote support and beam member, respectively; whilst, M, N and Q are generalised stresses.

The effective strain ϵ_{eff} can be expressed as follows

$$\epsilon_{\text{eff}} = \begin{cases} 2\left(\frac{W_B}{L}\right)^2\left(\frac{x}{L}\right)^2 + \left(\frac{W_B}{L}\right)\left(\frac{x}{L}\right)\left(\frac{H}{L}\right) & \text{if } 0 \leq x < L \\ \sqrt{\left[2\left(\frac{W_B}{L}\right)^2 + \left(\frac{W_B}{L}\right)\left(\frac{H}{L}\right)\right]^2 + \frac{1}{3}\left(\frac{W_S}{H}\right)^2} & \text{if } x = L \end{cases} \tag{1}$$

where W_B and W_S are transverse displacement at the mid-span of the beam and plastic shear sliding distance at the support, respectively; H is thickness and L is half length of the beam.

Initiation of ductile damage follows a criterion given by

$$\omega_d = \frac{\epsilon_{\text{eff}}}{\epsilon_d} = 1 \tag{2}$$

where ω_d is a state variable that increases monotonically with effective strain ϵ_{eff}, and ϵ_d is the effective strain at damage initiation (or damage strain). Beyond this, progressive softening of the generalised stresses occur in accordance to the following evolution law:

$$|\bar{M}| = |\bar{M}^f|(1-D), \quad \bar{N} = \bar{N}^f(1-D) \quad \text{and} \quad \bar{Q} = \bar{Q}^f(1-D) \tag{3}$$

where $\bar{M} = M/M_0$, $\bar{N} = N/N_0$ and $\bar{Q} = Q/Q_0$ are the non-dimensional fully plastic generalised stresses; $M_0 = \sigma_Y BH^2/4$, $N_0 = \sigma_Y BH$ and $Q_0 = 2\sigma_Y BH/3\sqrt{3}$ are the fully plastic bending moment, in-plane membrane force and transverse shear force, respectively; $\bar{M}^f$, $\bar{N}^f$ and $\bar{Q}^f$ are the non-dimensional generalised stresses at the onset of damage, respectively; σ_Y is the static yield strength; and, B is the width of the beam. The model assumes, for simplicity, a linear evolution of the damage variable D with effective strain ϵ_{eff} given by

$$D = \frac{\epsilon_{\text{eff}} - \epsilon_d}{\epsilon_r - \epsilon_d} \tag{4}$$

where ϵ_r is the rupture strain of the beam material. All the generalised stresses reduce to zero when $D = 1$ at which point *failure* (or complete severance from its supports) occurs. If the structural system fails before all its initial kinetic energy is expended, then the severed beam member would acquire a residual kinetic energy at the point of severance. Parts of this are absorbed through further plastic deformation as the beam continues to deform until it reaches a rigid permanent set whilst the remaining as translational kinetic energy. However, the current analytical model does not consider how this residual kinetic energy is expended beyond failure – it is not required for the purpose of this work.

The three distinct deformation régimes identified by Menkes and Opat (1973) are delineated according to the following criteria:

$$\text{Mode I}: \quad D < 1, \quad \omega_s < 1 \tag{5a}$$

$$\text{Mode II}: \quad D = 1, \quad \omega_s < 1 \tag{5b}$$

$$\text{Mode III}: \quad D = 1, \quad \omega_s \geq 1 \tag{5c}$$

where the state variable ω_s is given by

$$\omega_s = \frac{\beta}{\beta_c}. \tag{6}$$

In Eq 6, β is the ratio of the plastic work absorbed through shearing deformation to the total plastic work done and β_c (=0.45) is a critical value delineating the transition between modes II to III. Table 1 lists the material properties for the Aluminium 6061-T6 beams that were modelled; they are rate-insensitive.

It must be emphasised that we have adopted the term 'deformation régimes (or modes)' in place of the more widely-used 'damage régimes (or modes)' in conventional literature. This is to avoid unnecessary confusion associated with use of a damage variable D (Eq. 5) and the state variable ω_s (Eq. 6) as criteria to delineate different modes of deformation.

Table 1: Material properties of the Aluminium (6061-T6) beam (Menkes and Opat, 1973)

Density, ρ (kg/m^3)	Young's modulus, E (GPa)	Static yield strength, σ_Y (MPa)	Poisson's ratio	Damage strain, ϵ_d	Rupture strain, ϵ_r
2686	69	283	1/3	0.38	0.5

2.2. Generating pulse-pressures with varying negative phase

The ductile beam model of Yuan et al. (2016) is sufficiently general to accommodate different pressure profiles $p(t)$ such as linearly-decaying, triangular, rectangular etc – it had also been adapted to study fluid-structure interactions in underwater explosions (Yuan et al., 2017) and air blasts (Yuan et al., 2018). Here, the 'modified Friedlander equation' (Friedlander, 1946; Baker, 1973) will be used to generate the pulse-pressure $p(t)$, allowing both positive and negative phases of a blast pulse to be captured, as follows:

$$p(t) = p_0(1 - \frac{t}{t_d})e^{-\frac{\alpha t}{t_d}}, \quad 0 < t < \infty \tag{7}$$

where p_0 is peak value of the positive overpressure, t_d is duration of the positive phase and α ($\alpha \geq 0$) is the decay coefficient that determines the pulse-shape. Note that $\alpha = 0$ gives a linearly-decaying pressure pulse; whilst $\alpha > 0$ gives an exponentially decaying pressure-time history with differing severity of its negative phase that depends on α.

Figure 3a plots the pressure time-history for different decay coefficient α ranging from 0 to 5. In every curve, the pressure decays monotonically to zero at time $t = t_d$ - this is known as the positive phase of a blast pulse. It is then followed by a period of under-pressure – 'negative suction phase' – before pressure recovery to zero at time $t = t_d + t_d^-$, with the notable exception of $\alpha = 0$ where there is no negative phase, in other words, $t_d^- = 0$. Integrating Eq. 7 with respect to time, gives the positive I^+ and negative I^- impulses as follows:

$$I^+ = \int_0^{t_d} p(t)\mathrm{d}t = \begin{cases} I_0/2 & \text{if } \alpha = 0 \\ I_0(\mathrm{e}^{-\alpha} + \alpha - 1)/\alpha^2 & \text{if } \alpha > 0 \end{cases} \tag{8}$$

and

$$I^- = \int_{t_d}^{\infty} p(t)\mathrm{d}t = \begin{cases} 0 & \text{if } \alpha = 0 \\ -I_0\mathrm{e}^{-\alpha}/\alpha^2 & \text{if } \alpha > 0 \end{cases} \tag{9}$$

where $I_0 = p_0 t_d$ is the reference impulse. α is a critical parameter that controls the proportion of negative impulse (of the negative phase) to positive impulse (corresponding to the positive phase) for a given $p(t)$ (Baker et al., 1983). Figure 3b shows how the impulses corresponding to I^+ and I^- changes with α. Notice that the overall impulse $I^+ + I^-$ does not increase monotonically with α because of how its corresponding I^+ and I^- changes. In this paper,

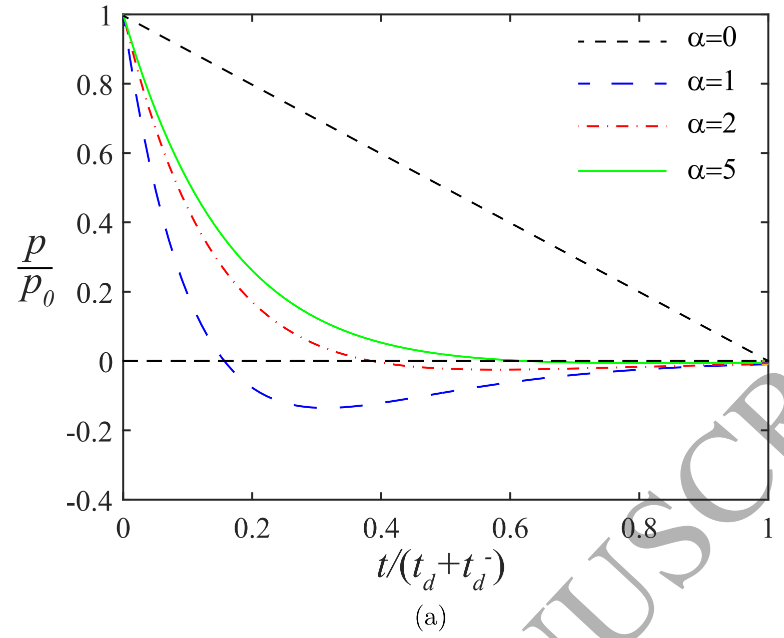

(a)

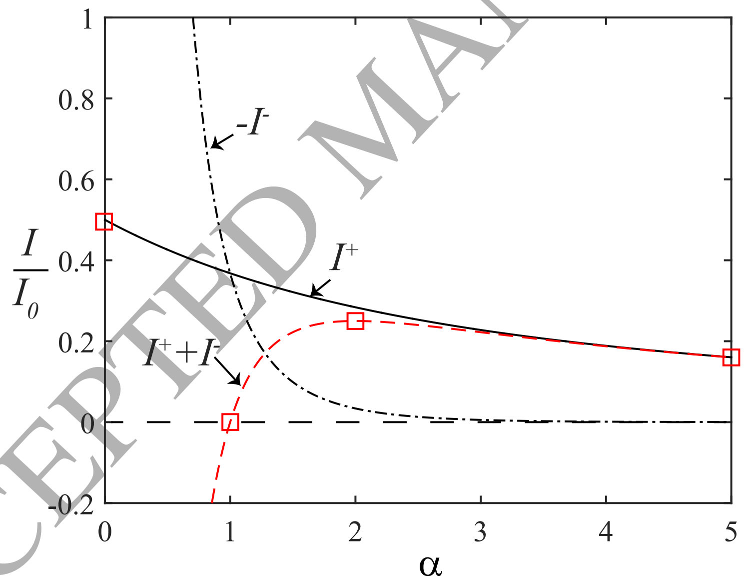

(b)

Figure 3: (a) Non-dimensional pressure time-history for different decay coefficients α; (b) corresponding impulses of the positive and negative phases of each pressure-time history in (a). Time $t_d + t_d^-$ corresponds to the instant when the non-dimensional pressure in the negative suction phase reaches $p/p_0 = -10^{-3}$.

129 the values of $\alpha = 0, 1, 2, 5$ were chosen for the following reasons: $\alpha = 0$ corresponds to an
130 extreme case of linear decaying profile; $\alpha = 1$ gives the most realistic pressure profile which
131 is supported by experimental evidence (Jacinto et al., 2001); and, $\alpha = 2$ and 5 are included

for the purpose of comparison.

In general, the pulse-pressure generated in a blast can be crudely classified as either *impulsive* (i.e. $t_3 > t_d$) or *non-impulsive* (i.e. $t_3 \leq t_d$). This depends on whether the time $t = t_3$, corresponding to either cessation of beam motion (for mode I) or failure (in modes II or III deformation), occurs after (i.e. $t_3 > t_d$) or before (i.e. $t_3 \leq t_d$) the end of the positive phase. Intuitively, it is obvious that the negative phase should only affect the maximum transient deflection of a beam subjected to impulsive loading, and only for a finite duration of $t_3 - t_d$ according on the aforesaid criteria to delineate the two loading régimes. Therefore, it is unnecessary to incorporate the impulse corresponding to the entire negative phase (I^-) when constructing a pressure-impluse diagram. In light of this, it is reasonable to choose the positive peak overpressure p_0 and positive impulse I^+ as the parameters to define the loading parameters space, which can be non-dimensionalised as follows:

$$p^* = \frac{p_0}{p_c} \tag{10}$$

and

$$I^* = \frac{I^+}{H\sqrt{\sigma_Y \rho}} \tag{11}$$

where $p_c = 4M_0/L^2$ is the fully plastic collapse force per unit length (Jones, 2012). Even though the negative impulse I^- is omitted from the p^*-I^* diagram, it is instructive to note that it is easily deduced using the following ratio (by re-arranging Eqs. 8 and 9)

$$\frac{I^-}{I^+} = -\frac{e^{-\alpha}}{e^{-\alpha} + \alpha - 1}, \quad \text{for } \alpha > 0. \tag{12}$$

The extent to which negative phase loading affects the structural performance of a ductile beam in the impulsive régime of a p-I diagram is to be discussed later in section 4.4.

2.3. *Justifications of assumption*

In this paper, we are concerned primarily with pulse-pressure loadings that are sufficiently intense to cause beam severance from its supports. If severance does not occur during the initial forward motion of a beam, then its subsequent temporal mid-point response, irrespective of whether negative phase loading is considered, would typically resembles that shown in Fig. 4 (see [- - -] and [- - -]), where the first peak corresponds to the maximum mid-span deflection and the first trough is a consequence of elastic rebound. This subsequent partial unloading and re-loading eventually dies out due to material damping. Results of three-dimensional FE simulations plotted in Fig. 4 were obtained, using an identical numerical set-up described in Yuan et al. (2016), for a beam with geometric and loading parameters given in the caption. Note that the vertical dashed red line [- - -] denotes the end of the positive loading phase (at $t/t_d = 1$). The pressure pulses (with and without negative phase) were imposed on the structure without considering fluid-structure interactions (Yuan et al., 2017, 2018) but this is not expected to alter the qualitative trend of the results shown here.

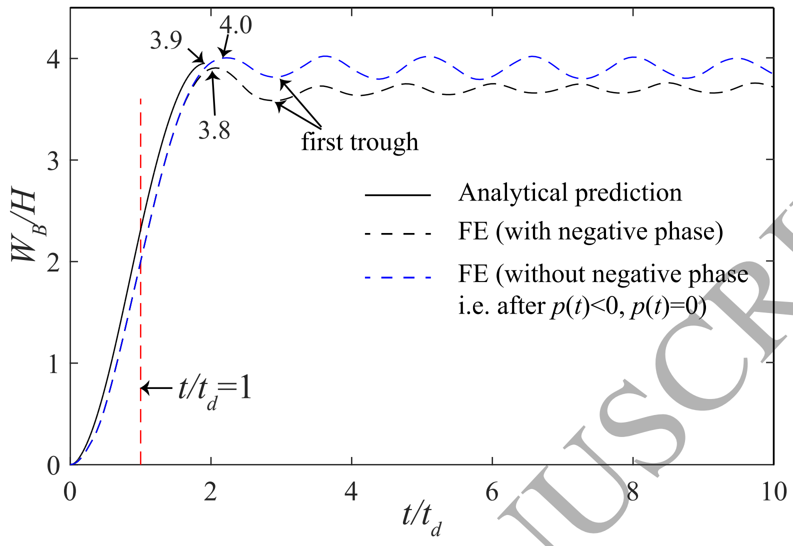

Figure 4: Comparison of analytical and FE predictions of the temporal mid-span deflection of a beam. The beam has dimensions of 0.203 ($2L$) $\times$ 6.35 $\times 10^{-3}$ (H) $\times$ 25.4 $\times 10^{-3}$ (B) m and is subjected to a pulse-pressure loading of $\alpha = 1$, $p^* = 20$ and $I^* = 0.37$.

Figure 4 shows that the analytical prediction [——] of the maximum mid-span deflection by Yuan et al. (2016) – a pulse-pressure with negative phase loading was imposed – is in good agreement with the results by FE ([- - -] and [- - -]). It is clear that the presence of negative phase loading has an effect of increasing the displacement of the first trough relative to the initial peak; however, this effect is relatively minor and it can reasonably be assumed that if a beam survives its initial forward motion without severance, then it is unlikely to fail in the subsequent reverse motion. Since the primary concern of this work is to construct régime boundaries, corresponding to modes I→II and II→III, that involves beam severance, the analytical model by Yuan et al. (2016) is applicable here even though it did not consider unloading and re-loading effects associated with elastic rebound.

3. Pressure-impulse diagrams

3.1. Key features of p^*-I^* diagram

Figure 5 presents a p^*-I^* diagram for a typical aluminium (6061-T6) beam tested by Menkes and Opat (1973). Here, as in Shen and Jones (1992) and Yuan et al. (2016), a linear-decaying pressure pulse with $\alpha = 0$ is used which considers only a positive phase. Two isodamage curves divide the p^*-I^* space into deformation régimes (mode I: large inelastic deformation; mode II: tensile-tearing at the support; mode III: shear-band localisation) that develop in

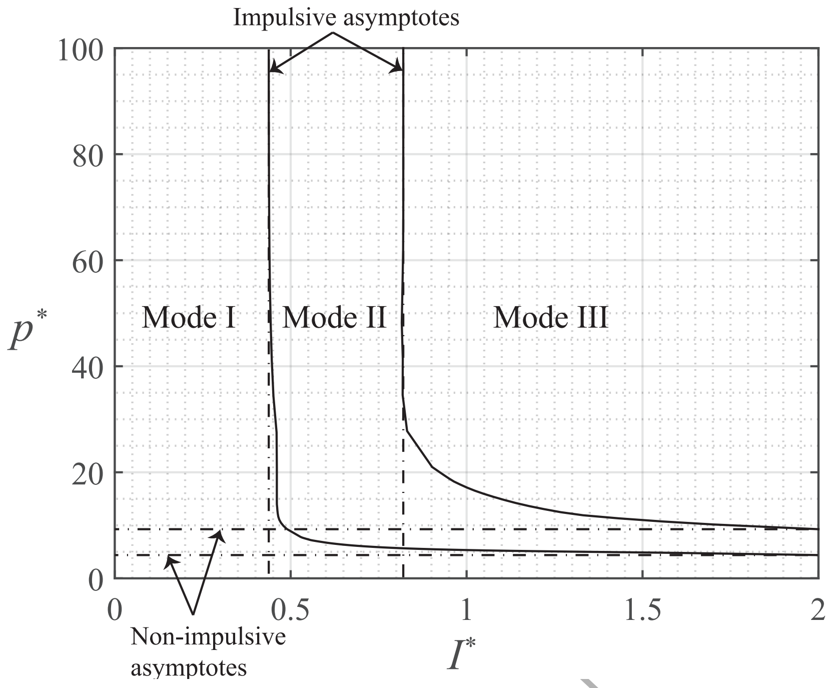

Figure 5: A p^*-I^* diagram that divides the loading parameters space into deformation régimes (modes I, II and III) for a typical aluminium beam (0.203 ($2L$) $\times$ 6.35 $\times 10^{-3}$ (H) $\times$ 25.4 $\times 10^{-3}$ (B) m) tested in Menkes and Opat (1973). -.-.- indicates the impulsive and non-impulsive asymptotes.

ductile beams under blast loading. Each isodamage curve shares broadly similar features to existing p-I diagrams in the literature which, unlike the present study, uses a simple maximum deflection criterion (SDOF model) to construct their boundaries (Li and Meng, 2002a) as follows: (1) there is a vertical and a horizontal asymptote that corresponds to an impulsive and a non-impulsive loading régime, respectively (they are often known as *impulsive* and *non-impulsive* asymptotes); and (2) between these two asymptotes, there is a one-to-one correspondence between p^* and I^* for any monotonically decaying pressure pulse. In addition, the predicted impulsive asymptotes correspond to the critical non-dimensional impulses for mode I$\rightarrow$II and II$\rightarrow$III transitions (0.44 and 0.82, respectively) and they agree well with existing experimental results (0.49 and 0.87, respectively) in Menkes and Opat (1973).

3.2. Effects of decay coefficient α

Figure 6 shows a typical non-dimensional p^*-I^* diagram for various decay coefficient α ranging from 0 to 5 for a beam of aspect ratio $L/H = 16$ (the beam has identical dimensions to the one in Fig. 5). Recall that $\alpha = 0$ corresponds to a linearly-decaying pressure pulse without a negative phase. It is instructive to note that the magnitude of the negative phase impulse I^- (using Eq. 12) is -1, -0.12 and -0.002 times its positive counterpart for α=1, 2 and 5, respectively. In general, the presence of a negative phase leads to an expansion of the mode I régime space by shifting (or tilting) the impulsive asymptote (for mode I$\rightarrow$II transition)

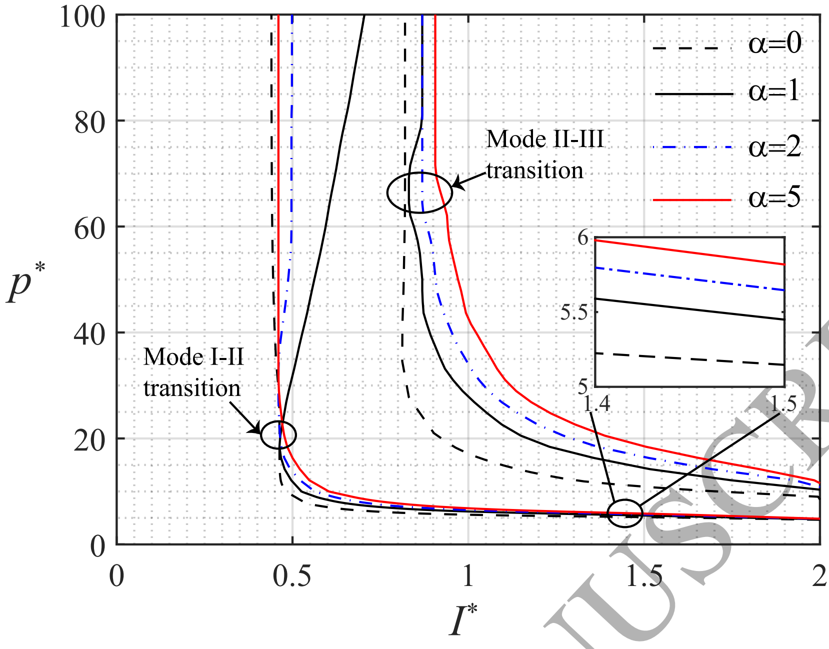

Figure 6: Non-dimensionalised p^*-I^* diagram for a beam subjected to a pulse-pressure with different values of α. The beam has dimensions of 0.203 ($2L$) $\times$ 6.35 $\times 10^{-3}$ (H) $\times$ 25.4 $\times 10^{-3}$ (B) m.

rightwards. This is because a negative loading phase decelerates the beam, leading to a lower maximum mid-span deflection compared to its linearly-decaying counterpart. Hence, the biggest shift in the mode I→II impulsive asymptote is observed for α=1 by virtue of its corresponding I^-; strictly speaking, they cannot now be regarded as an asymptote. On the other hand, increasing α leads to contraction of the mode III régime space caused by a shift ('diagonally' upwards) in the isodamage curve for II→III transition. Note that the two isodamage lines corresponding to $\alpha = 0$ define a lower bound for deformation régimes for all other pulse-pressures with a negative phase, i.e. $\alpha = 1, 2, 5$. It is worth emphasising that the negative impulse I^- is not reflected within the non-dimensionalised impulse p^*-I^* diagram but it is easily deduced using Eq. 12 once α (>0) is known.

Below are some observations regarding the sensitivity of the isodamage curve for mode I→II transition to α, as shown in Fig. 6:
(1) For $\alpha = 1$, the critical impulse I^* at mode I→II transition increases monotonically with p^* in the impulsive régime. By contrast, it remains an invariant if $\alpha = 0$ as shown in Fig. 5. As a result, for certain values of I^* (say 0.6), increasing the non-dimensional pressure p^*, say, from 20 to 80 switches the deformation mode of the beam from II→I, making it 'safer' (by remaining in mode I) when subjected to a pulse-pressure with a considerable negative phase. This is easily rationalised by noting that a beam is inevitably subjected to a period of negative phase loading in the impulsive régime (i.e. $t_3 > t_d$) that causes it to decelerate. Increasing p^* for a given I^* would allow the beam to enter the negative phase earlier (reducing t_d) resulting in a somewhat lower maximum beam deflection (this will be

shown later in Fig. 8) and less overall impulse transmitted to the beam (this will be shown later in Fig. 12).
(2) Increasing α (excluding the case of $\alpha = 0$) tilts the isodamage curve for the impulsive loading régime towards to the right, leading to an expansion of the mode I régime space, for reasons already given above.
(3) In the non-impulsive régime, however, reducing α leads to a contraction of the mode I régime space, see figure inset. As noted previously, this is not a consequence of the negative phase since the maximum beam deflection is reached before the end of the positive phase in the non-impulsive régime. Instead, it is due to the effects of pulse-shape. Increasing α leads to a reduction in the positive phase duration t_d for a given I^* (see Fig. 3b), which leads inevitably to a higher maximum beam deflection in mode I, and this is consistent with previous findings by Yuan et al. (2016) and Xue and Hutchinson (2003).

In general, the decay coefficient α affects both the negative phase and shape of a pressure pulse and they, in turn, have a significant influence over a beam's structural response in the impulsive and non-impulsive régime of a p^*-I^* diagram, respectively.

3.3. Effects of aspect ratio L/H

Figures 7a and 7b show p^*-I^* diagrams for beams of different aspect ratio L/H (but with identical cross-sectional area) subjected to a linearly decaying ($\alpha = 0$) and an exponentially decaying ($\alpha = 1$) pulse-pressure with negative phase, respectively. In both cases, the shifts in their isodamage lines within the p^*-I^* space are largely similar depending on L/H. As the aspect ratio of a beam increases, its impulsive asymptote (corresponding to the transition from mode I$\rightarrow$II) shifts leftward, whereas its non-impulsive counterpart shifts upward. The implication is that a longer beam would be 'safer' (remaining in mode I) when subjected to non-impulsive loading, but is more likely to lose its integrity at the support (in mode II) under impulsive loading. Reducing the aspect ratio of a beam tends to trigger an earlier onset of mode III deformation since transverse shear plays a dominant role in shorter beams whenever complete detachment occurs at its supports.

4. Design maps

In this section, we construct design maps that incorporate contour lines of structural performance (maximum deflection, total work done, partitioned energy and saturated impulse) into the non-dimensionalised pressure-impulse space. Any pair of p^* and I^* uniquely locates a point in the 2D space. From the map, one is able to determine the deformation régime in addition to information (by interpolation using two known values, if required) needed to assess structural performance. Alternatively, it enables a designer to determine the critical non-dimensional pressure p^* that delineates different deformation régimes, and the corresponding structural performance, for a given non-dimensional impulse I^*. These charts are potentially useful for the preliminary blast assessment of structures by designers. All results

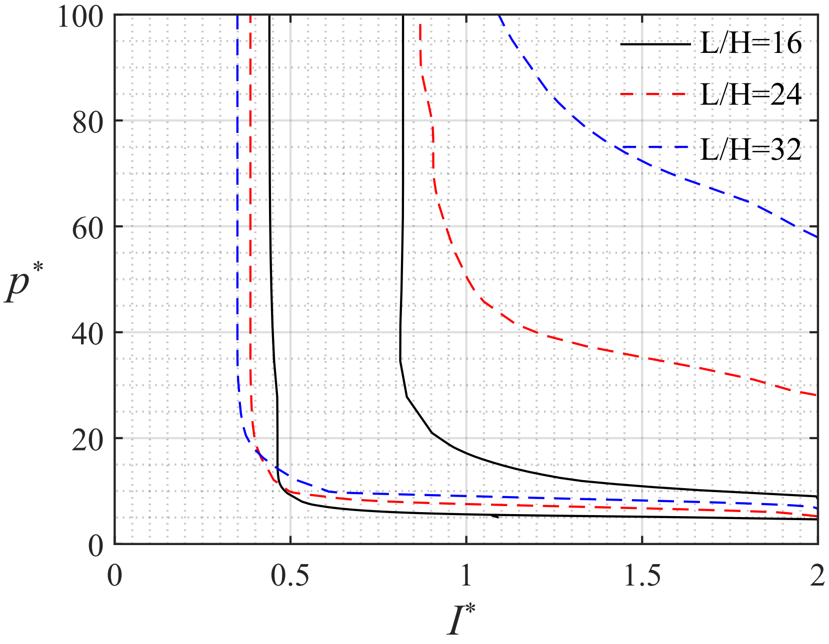

(a) $\alpha = 0$

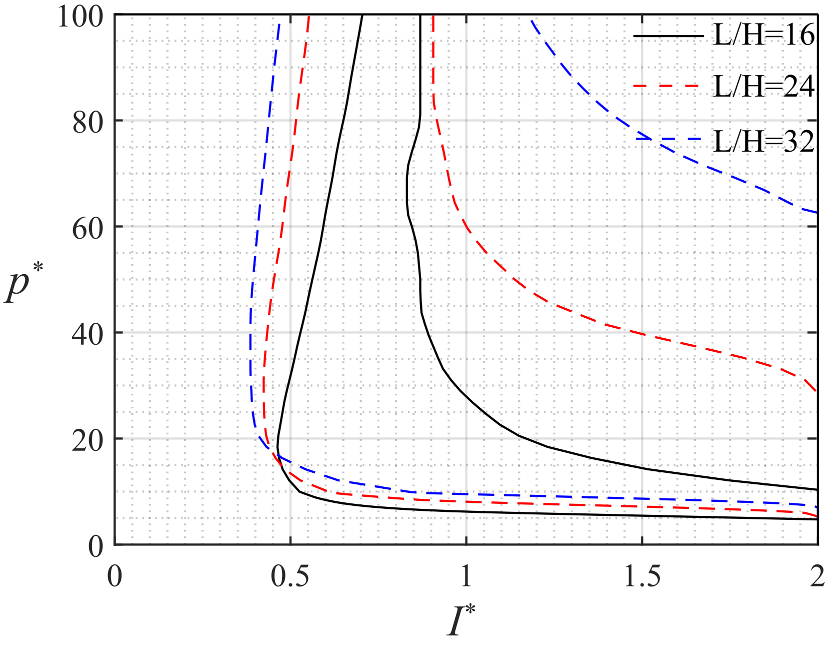

(b) $\alpha = 1$

Figure 7: p^*-I^* diagrams for beams of different L/H but with identical cross-sectional area of 6.35 $\times 10^{-3}$ (H) m $\times$ 25.4 $\times 10^{-3}$ (B) m.

shown are for beams of dimensions 0.203 ($2L$) $\times$ 6.35 $\times 10^{-3}$ (H) $\times$ 25.4 $\times 10^{-3}$ (B) m subjected to either a linearly-decaying ($\alpha = 0$) or an exponentially decaying pulse-pressure ($\alpha = 1$) pressure pulse.

4.1. Transverse mid-span deflection and plastic shear sliding distance

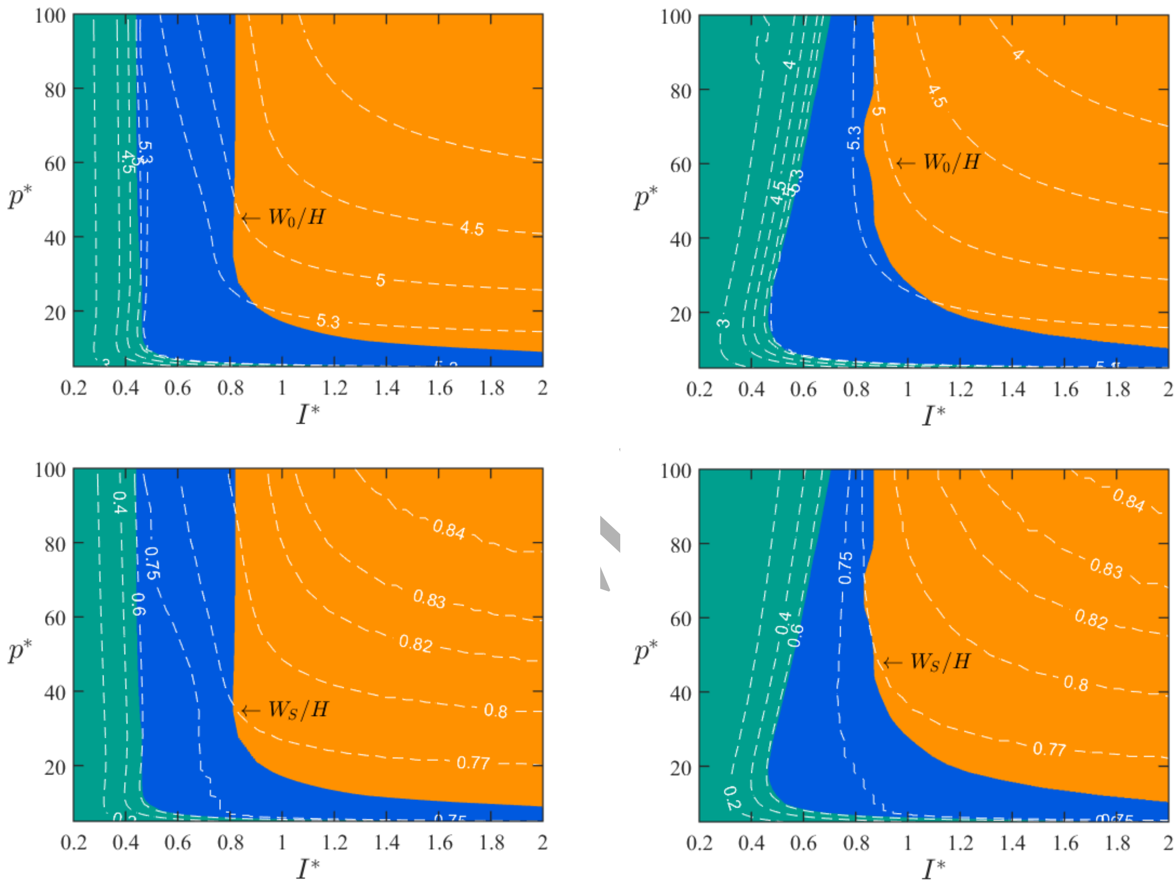

(a) $\alpha = 0$ (b) $\alpha = 1$

Figure 8: Contours of non-dimensional maximum deflection W_0/H and plastic shear sliding distance W_S/H superimposed on the loading parameters space for (a) $\alpha = 0$ and (b) $\alpha = 1$. ■ mode I; ■ mode II; ■ mode III.

Figures 8a and 8b show design maps that incorporates information on the non-dimensional transverse beam deflection – maximum mid-span deflection W_0/H and plastic shear sliding distance W_S/H at the support – within the p^*-I^* space for $\alpha = 0$ and $\alpha = 1$, respectively. In mode II and III régimes, increasing the non-dimensional pressure p^* (for a fixed I^*), or impulse I^* (for a fixed p^*), leads to a monotonic reduction of W_0/H and a monotonic increase of W_S/H. Furthermore, Fig. 8b shows that for certain I^* (say $I^* = 0.6$), reducing the non-dimensional pressure p^* from, say, 80 to 20 would have led to a higher mid-span deflection of W_0/H and plastic shear sliding distance W_S/H. This explains the shift in deformation régime from mode I $\rightarrow$ II alluded to earlier in Fig. 6 - see Section 3.2.

It is interesting to note that the contour corresponding to $W_0/H = 5.3$ in Figs. 8a and 8b is nearly coincident with the isodamage curve for mode I$\rightarrow$II transition. This is consistent with the findings of Yuan et al. (2016) and Shen and Jones (1992) where it had been shown that the maximum W_0/H is reached during the transition from mode I$\rightarrow$II. Therefore, a simple maximum displacement failure criterion (as is commonly employed in the literature) is equally capable of predicting the same isodamage curve for mode I$\rightarrow$II transition compared to the damage criterion (Eqs. 5b) used here. However, the maximum displacement failure criterion in existing literature cannot accurately predict W_0/H beyond its mode I$\rightarrow$II transition as the beam is considered to have failed at the same maximum displacement.

4.2. External work done

We introduce a non-dimensional transmitted energy from the pulse-pressure to the beam system – defined as the ratio of the external work done to the beam E^P to the reference energy E^+ – as follows:

$$\bar{E}^P = \frac{E^P\left(\triangleq \int_0^{t_3} p(t)\left[\int_0^L \dot{W}(x,t)\mathrm{d}x\right]\mathrm{d}t\right)}{E^+\left(\triangleq (I^+)^2/2m\right)} \tag{13}$$

where time $t = t_3$ corresponds to either the cessation of beam motion or at the instant of failure (i.e. complete detachment from the supports). It is instructive to note that the ratio $\bar{E}^P$ provides a measure of the 'impulsiveness' in a beam's response, with $\bar{E}^P = 1$ corresponding to the extreme case of a 'zero-period' impulsive loading where the structure may be assumed to acquire an instantaneous velocity. Contour plots of $\bar{E}^P$ is incorporated into the loading parameters space, for $\alpha = 0$ and $\alpha = 1$, in Figs. 9a and 9b. It is evident that either increasing I^* or reducing p^* causes the beam to respond in an increasingly 'non-impulsive' manner and has a dramatic effect of reducing (monotonically) the energy transmitted to the beam by the pulse-pressure loading. In addition, for the same combination of p^* and I^*, $\bar{E}^P$ is smaller for $\alpha = 1$ (Fig. 9b) compared to $\alpha = 0$ (Fig. 9a). This is unsurprising since negative phase loading in an exponentially decaying pressure pulse ($\alpha = 1$) produces 'negative' increment of work, leading to less external work done on the structure compared to its linearly-decaying counterpart.

4.3. Partitioning of energy

The components of plastic work absorbed at the *supports* through bending, membrane stretch and shear can be non-dimensionalised as follows:

$$\bar{E}_S^b = \frac{E_S^b}{E_S^s + E_S^b + E_S^m}, \quad \bar{E}_S^m = \frac{E_S^m}{E_S^s + E_S^b + E_S^m}, \quad \text{and} \quad \bar{E}_S^s = \beta = \frac{E_S^s}{E_S^s + E_S^b + E_S^m} \tag{14}$$

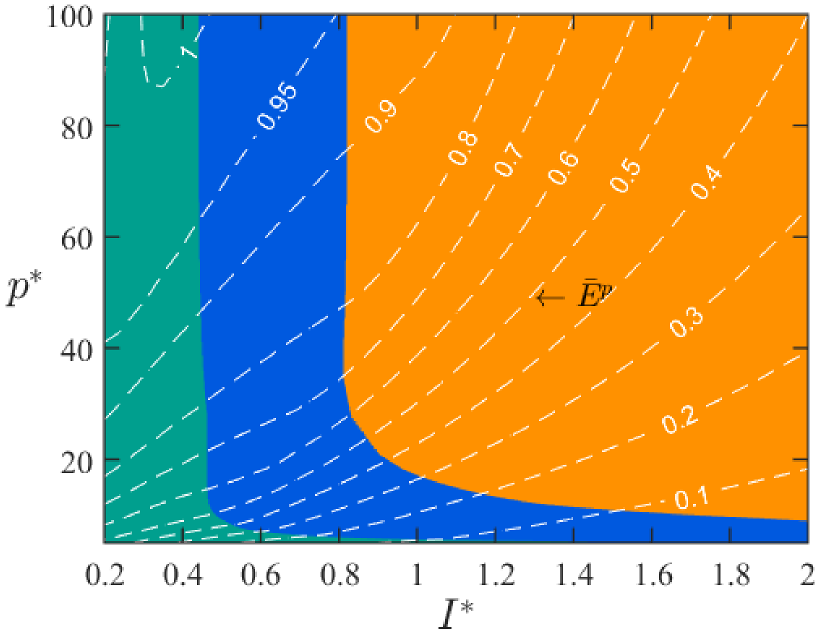

(a) $\alpha = 0$

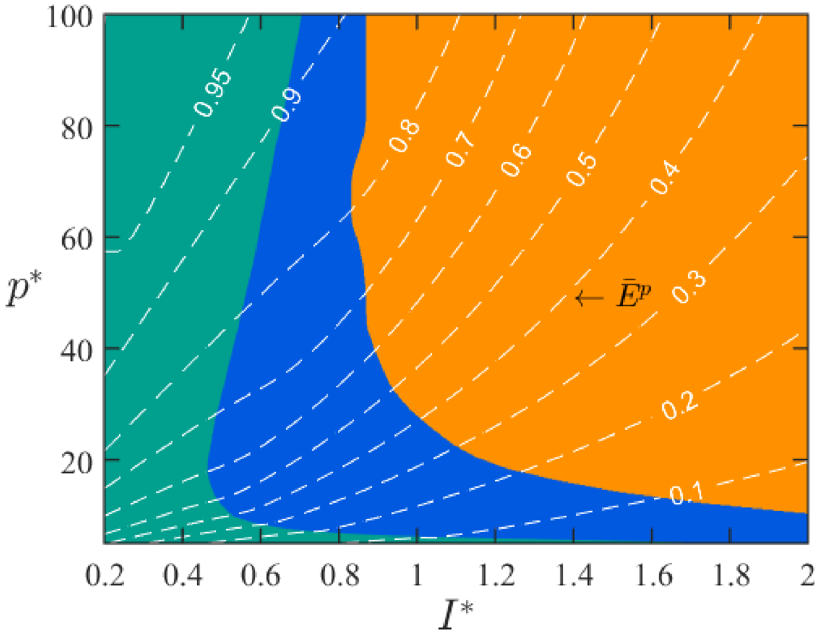

(b) $\alpha = 1$

Figure 9: Contours of non-dimensional external work done $\bar{E}^P$ super-imposed on the loading parameters space for (a) $\alpha = 0$ and (b) $\alpha = 1$. ■ mode I; ■ mode II; ■ mode III.

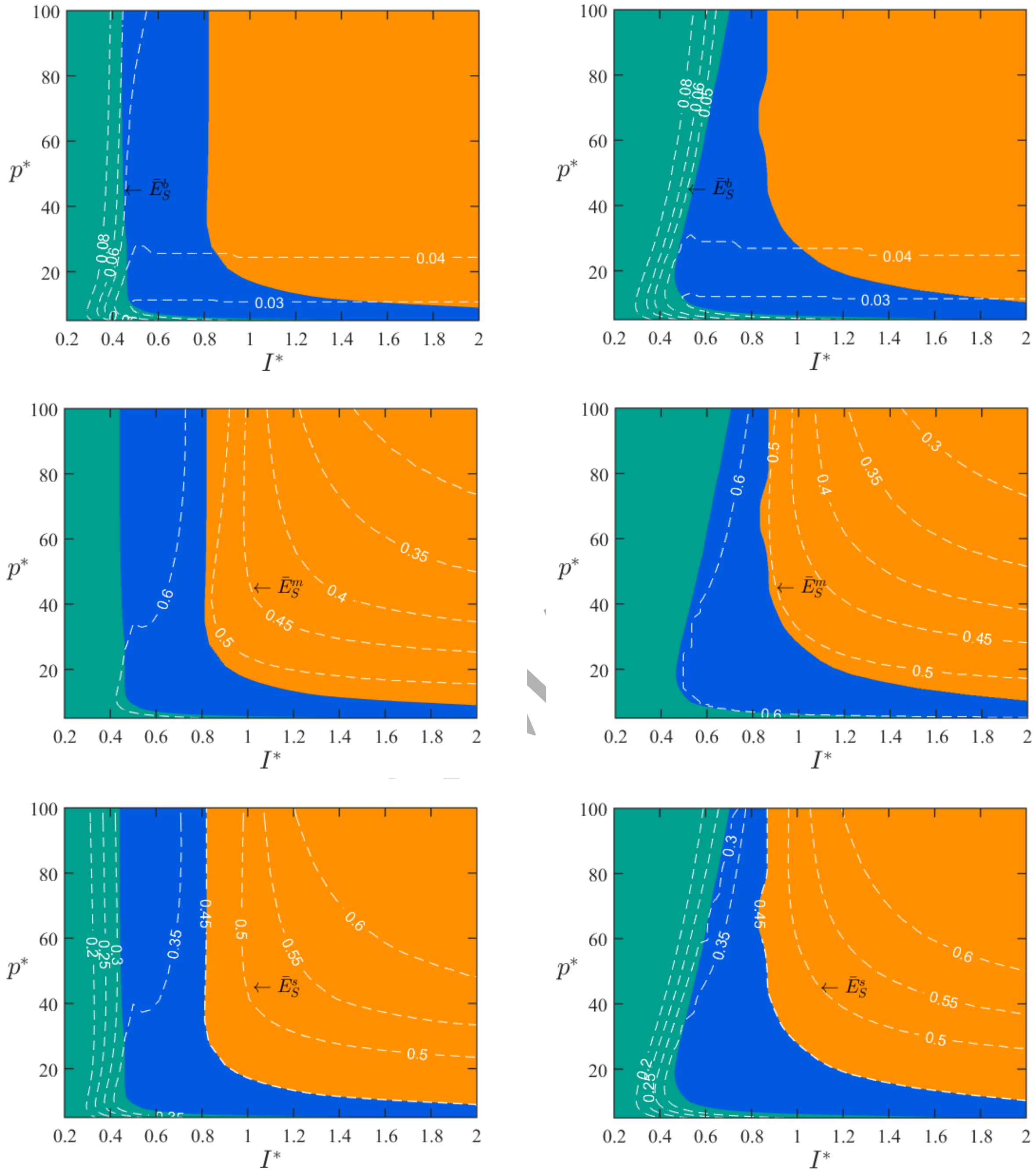

(a) $\alpha = 0$ (b) $\alpha = 1$

Figure 10: Contours of non-dimensional plastic energy absorbed at the support through bending $\bar{E}_S^b$, membrane stretch $\bar{E}_S^m$ and transverse shear displacement $\bar{E}_S^s$ superimposed on the loading parameters space. ■ mode I; ■ mode II; ■ mode III.

where E_S^s, E_S^b and E_S^m are, respectively, the shear, bending and membrane strain energies absorbed at the supports. Note that $\bar{E}_S^b + \bar{E}_S^m + \bar{E}_S^s = 1$. Figures 10a and 10b plot contours of the three components of plastic work at the supports for $\alpha = 0$ and $\alpha = 1$. It is evident from both figures that membrane stretch and transverse shear play key roles in inducing modes II and III deformation, with negligible contributions from bending - this is consistent with existing literature (Yuan et al., 2016; Yu and Chen, 2000; Li and Jones, 2000; Shen and Jones, 1992). In mode III, reducing either p^* or I^* (or both) causes a monotonic increase of $\bar{E}_S^m$; the reverse occurs for $\bar{E}_S^s$. This is because a lower p^* or I^* would result in a higher mid-span deflection W_0/H and a lower plastic sliding distance W_S/H (as seen previously in Fig. 8), leading to a higher energy absorbed through membrane stretch and a lower energy dissipated through transverse shear, respectively.

4.4. Saturated impulse

Since the non-dimensional impulse in the p^*-I^* space is expressed as a function of the positive impulse I^+ in Eq 11, it does not provide a true measure of the actual impulse imparted to the beam. This is because any further loading after the cessation of beam motion, or beyond complete failure (detachment from supports), would not increase a beam's maximum transverse deflection. Hence, it can be misleading if one uses the peak overpressure p_0 and positive impulse I^+ in design since the actual impulse that affects permanent deformation could be less than the positive impulse I^+. This is known as a '*saturation phenomenon*'. The physical origin of this phenomenon was first investigated by Zhao et al. (1994) and Zhu and Yu (1997): since the load-carrying capacity of a beam or plate is greatly enhanced by the membrane forces induced by large deflection and if it is subjected to a pressure pulse with a sufficiently long duration, only an early part of the pulse contributes to its maximum deflection; the rest of the loading pulse causes no further increase. A series of papers – Zhao et al. (1994, 1995), Zhu and Yu (1997), Zhu et al. (2017), Bai et al. (2018) – have extensively documented this saturation phenomenon, including saturated deflection and saturated impulse, for various pulse shapes and different structural elements.

Here, we define the saturated impulse I_{sat} as the critical impulse beyond which the deflection of a beam would no longer increase under further loading given by

$$I_{\text{sat}} = \int_0^{t_3} p(t)\mathrm{d}t \tag{15}$$

and this is the impulse imparted to the beam before it reaches maximum deflection. Again, it is worth emphasising that, at the point of severance (in modes II or III), a beam is assumed to have reached its maximum transverse deflection – this is a consequence of the model assumption. In reality, its transverse deflection could increase after severance if it had acquired sufficient residual kinetic energy. Here, however, we are only concerned with

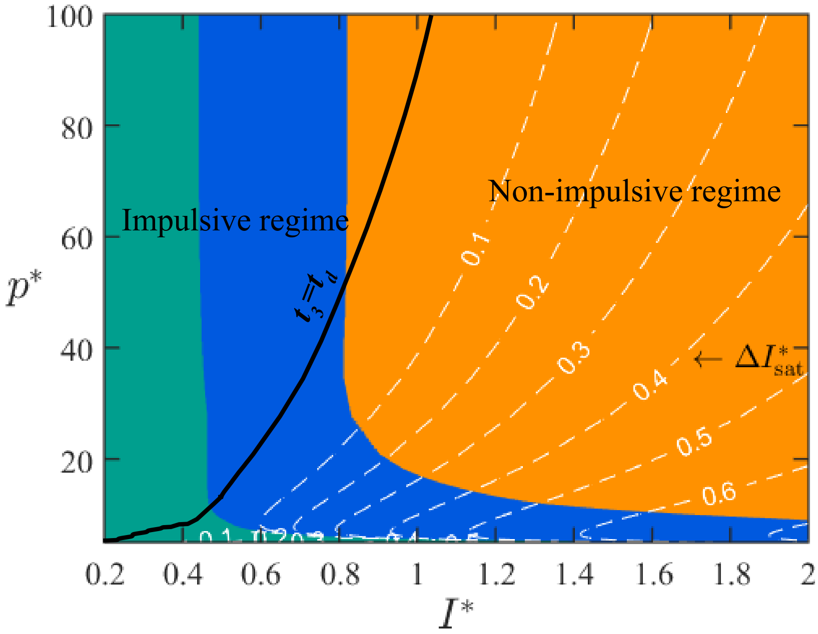

(a) $\alpha = 0$

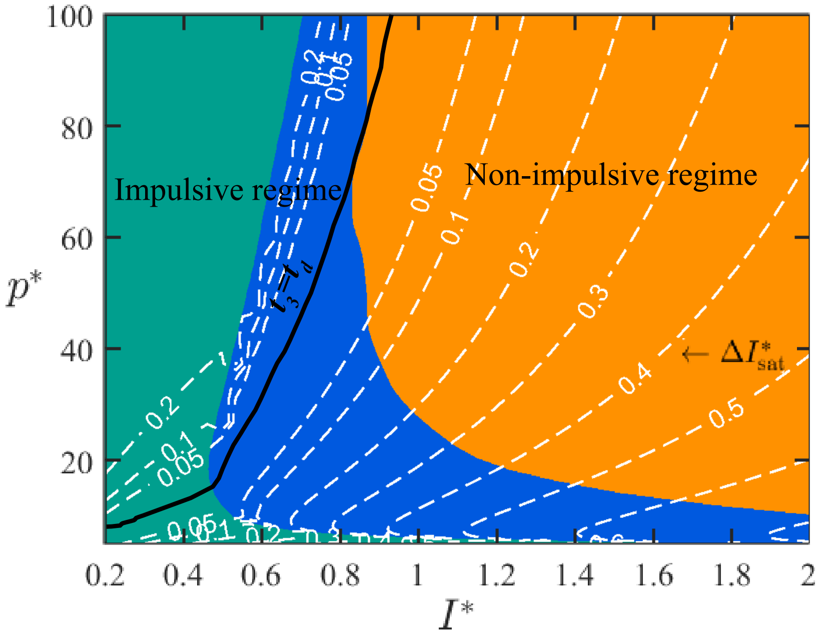

(b) $\alpha = 1$

Figure 11: Contours on error (ΔI^*_{sat}) that would arise if saturation phenomenon is ignored. ■ mode I; ■ mode II; ■ mode III.

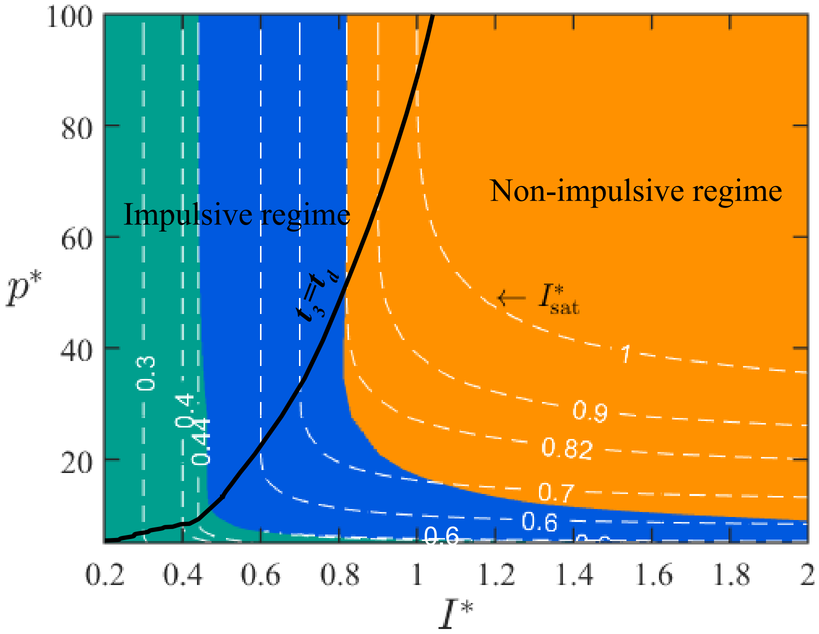

(a) $\alpha = 0$

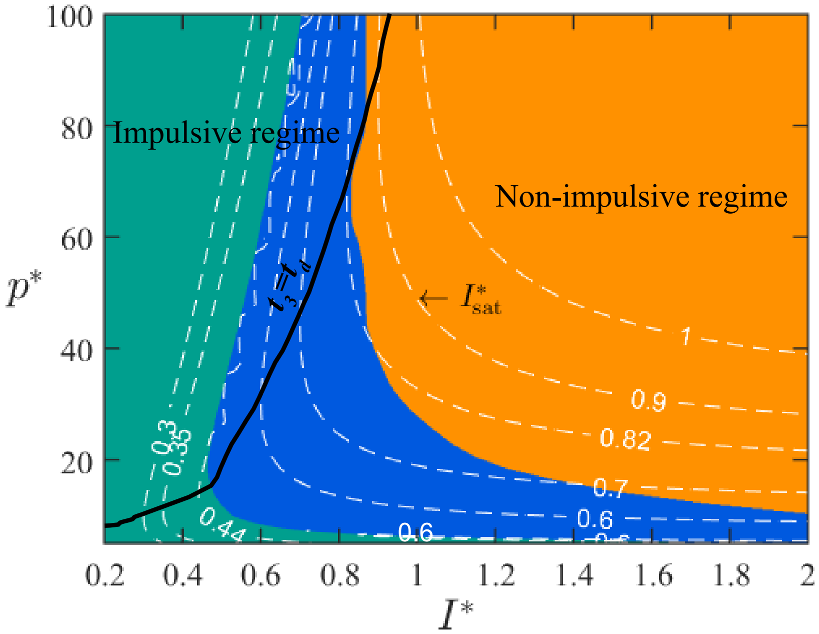

(b) $\alpha = 1$

Figure 12: Contours of non-dimensional saturated impulse $I^*_{\rm sat}$ superimposed on the loading parameters space. ■ mode I; ■ mode II; ■ mode III.

the maximum deflection at the point of severance. The saturated impulse can be non-dimensionalised as follows:

$$I_{\rm sat}^* = \int_0^{t_3} \frac{p(t)}{H\sqrt{\sigma_Y \rho}}\,{\rm d}t. \tag{16}$$

It is worth noting that a saturation phenomenon is only observed if $I^* > I_{\rm sat}^*$; hence, it is helpful to define a ratio

$$\Delta I_{\rm sat}^* = \frac{I^* - I_{\rm sat}^*}{I^*}, \tag{17}$$

as a measure of the error that would arise if saturation phenomenon is not considered when calculating the maximum beam deflection. $\Delta I_{\rm sat}^*$ must be greater than zero; otherwise, impulse saturation does not occur.

Contours of $\Delta I_{\rm sat}^*$ are embedded into the p^*-I^* space in Figs. 11a and 11b. Likewise, its corresponding non-dimensional saturated impulse $I_{\rm sat}^*$ are shown in Figs. 12a and 12b. The locus of points connecting $t_3 = t_d$ now divides the pressure-impulse space into an impulsive ($t_3 > t_d$) and a non-impulsive ($t_3 \leq t_d$) régime. Notice that both régimes span all three modes of deformation. It is evident from Figs. 11a and 11b that a saturation phenomenon can only exists (since $\Delta I_{\rm sat}^*$ needs to be greater than zero) in the non-impulsive régimes if $\alpha = 0$ as expected; by contrast, it can occur in either régimes if $\alpha = 1$. It is instructive to note that $\Delta I_{\rm sat}^*$ in impulsive régime (see Fig 11b) provides a measure of the non-dimensional negative impulse imparted to the beam, this causes it to decelerate, which result in a non-vertical impulsive asymptote discussed earlier in Fig. 6. In general, the further a pair of p^*-I^* is located from the locus of points connecting $t_3 = t_d$, the greater will be the error that would arise if impulse saturation is not taken into account - this applies to both $\alpha = 0$ and $\alpha = 1$.

Figures 12a and 12b reveal that the non-dimensional saturated impulse $I_{\rm sat}^*$ is discontinuous across the boundary separating modes I and II. The critical $I_{\rm sat}^*$ is 0.44 in the impulsive régime and 0.6 in the non-impulsive régime. Interestingly, both critical values are independent of α, i.e. they are pulse-shape insensitive. The reason why the critical $I_{\rm sat}^*$ is higher in the non-impulsive régime (0.6) compared to its impulsive counterpart (0.44) because, for a given saturated impulse, a beam subjected to impulsive loading will always have a higher maximum deflection compared to its non-impulsive counterpart (Xue and Hutchinson, 2003; Yuan et al., 2016). Although the deflection W_0/H in mode III is, in general, less than in mode II (comparing Figs. 8a and 8b), it necessitates a greater saturated impulse to induce a mode III deformation; this is evident by comparing $I_{\rm sat}^*$ in mode III to that in mode II régime).

5. Conclusions

Non-dimensional p^*-I^* diagrams were developed for a beam of 0.203 ($2L$) $\times$ 6.35 $\times 10^{-3}$ (H) $\times$ 25.4 $\times 10^{-3}$ (B) m, by using a more realistic structural model, that separates the loading parameter space in accordance to the modes of deformation observed in blast experiments. It was found that the isodamage curves, delineating the régimes, are sensitive to the decay coefficient α and aspect ratio L/H of the beam. The two isodamage curves corresponding to $\alpha = 0$ define a lower bound for deformation régimes for all other pulse-pressures with a negative phase. Reducing the decay coefficient α or aspect ratio L/H leads to greater margin of safety (i.e. the beam remains in mode I) under impulsive loading; while the reverse occurs for non-impulsive loading. Increasing α or L/H has the dramatic effect of shrinking the loading parameter space associated with mode III deformation régime. In addition, it was demonstrated that contour lines of structural performance (maximum deflection, total work done, partitioned energy and saturated) can also be incorporated into the non-dimensionalised pressure-impulse space to provide further information for the design, and assessment, of structures to blast loading.

Acknowledgment

Ye Yuan and Yibing Li acknowledge the financial support from the National Science Foundation of China (Grants No. 11372164 and 11772176). PJ Tan acknowledges the financial support of QinetiQ (Mr Robert Ball - Structures & Survivability, Platform Design and Life Support IDT).

References

Abrahamson, G., Lindberg, H., 1976. Peak load-impulse characterization of critical pulse loads in structural dynamics. Nucl. Eng. Des. 37 (1), 35 – 46.

Bai, X., Zhu, L., Yu, T. X., 2018. Saturated impulse for fully clamped square plates under blast loading. Int. J. Mech. Sci. (AEPA2016 Special Issue) 146-147, 417 – 431.

Baker, W., Cox, P., Westine, P., Kulesz, J., Strehlow, R., 1983. Explosion hazards and evaluation. Amsterdam: Elsevier.

Baker, W. E., 1973. Explosions in Air. Austin: University of Texas Press.

Dragos, J., Wu, C., 2013. A new general approach to derive normalised pressure impulse curves. Int. J. Impact Eng. 62, 1 – 12.

Friedlander, F. G., 1946. The diffraction of sound pulses. i. diffraction by a semi-infinite plane. Proceedings of the Royal Society of London A: Mathematical, Physical and Engineering Sciences 186 (1006), 322–344.

Hamra, L., Demonceau, J.-F., Denoel, V., 2015. Pressure-impulse diagram of a beam developing non-linear membrane action under blast loading. Int. J. Impact Eng. 86, 188 – 205.

Jacinto, A. C., Ambrosini, R. D., Danesi, R. F., 2001. Experimental and computational analysis of plates under air blast loading. Int. J. Impact Eng. 25 (10), 927 – 947.

Jones, N., 2012. Structural Impact, 2nd Edition. Cambridge University Press.

Li, Q. M., Jones, N., 2000. Formation of a shear localization in structural elements under transverse dynamic loads. Int. J. Solids Struct. 37 (45), 6683 – 6704.

Li, Q. M., Meng, H., 2002a. Pressure-impulse diagram for blast loads based on dimensional analysis and single-degree-of-freedom model. J. Eng. Mech. 128 (1), 87–92.

Li, Q. M., Meng, H., 2002b. Pulse loading shape effects on pressure-impulse diagram of an elastic-plastic, single-degree-of-freedom structural model. Int. J. Mech. Sci. 44 (9), 1985 – 1998.

Ma, G. W., Shi, H. J., Shu, D. W., 2007. P-I diagram method for combined failure modes of rigid-plastic beams. Int. J. Impact Eng. 34 (6), 1081 – 1094.

Menkes, S., Opat, H., 1973. Broken beams. Exp. Mech. 13, 480–486.

Shen, W. Q., Jones, N., 1992. A failure criterion for beams under impulsive loading. Int. J. Impact Eng. 12 (1), 101 – 121.

Tsai, Y., Krauthammer, T., 2017. Energy based load-impulse diagrams. Eng. Struct. 149, 64–77.

Xue, Z., Hutchinson, J. W., 2003. Preliminary assessment of sandwich plates subject to blast loads. Int. J. Mech. Sci. 45 (4), 687 – 705.

Yu, T. X., Chen, F. L., 2000. A further study of plastic shear failure of impulsively loaded clamped beams. Int. J. Impact Eng. 24 (6-7), 613 – 629.

Yuan, Y., Tan, P. J., Shojaei, K. A., Wrobel, P., 2016. Large deformation, damage evolution and failure of ductile structures to pulse-pressure loading. Int. J. Solids Struct. 96, 320 – 339.

Yuan, Y., Tan, P. J., Shojaei, K. A., Wrobel, P., 2017. The influence of deformation limits on fluid-structure interactions in underwater blasts. Int. J. Impact Eng. 101, 9–23.

Yuan, Y., Tan, P. J., Shojaei, K. A., Wrobel, P., 2018. On momentum transfer and external work done to clamped elasto-plastic beams in an air blast. Int. J. Mech. Sci. 146-147, 377–385.

Zhao, Y. P., Yu, T. X., Fang, J., 1994. Large dynamic plastic deflection of a simply supported beam subjected to rectangular pressure pulse. Archive of Applied Mechanics 64 (3), 223–232.

Zhao, Y. P., Yu, T. X., Fang, J., 1995. Saturated impulses for dynamically loaded structures with finite-deflections. Structural Engineering and Mechanics 3 (6), 583–592.

Zhu, L., Bai, X., Yu, T. X., 2017. The saturated impulse of fully clamped square plates subjected to linearly decaying pressure pulse. Int. J. Impact Eng. 110, 198–207.

Zhu, L., Yu, T. X., 1997. Saturated impulse for pulse-loaded elastic-plastic square plates. Int. J. Solids Struct. 34 (14), 1709 – 1718.